Biosensors and Bioelectronics 152 (2020) 112006

Contents lists available at ScienceDirect

Biosensors and Bioelectronics

journal homepage: http://www.elsevier.com/locate/bios

The combination of ternary electrochemiluminescence system of g-C_3N_4 nanosheet/TEA/Cu@Cu_2O and G-quadruplex-driven regeneration strategy for ultrasensitive bioanalysis

Jia-Li Liu [a], Jie Jiang [a], Jia-Qi Zhang [a], Ya-Qin Chai [a], Qi Xiao [b,**], Ruo Yuan [a,*]

[a] Key Laboratory of Luminescent and Real-Time Analytical Chemistry (Southwest University), Ministry of Education, College of Chemistry and Chemical Engineering, Southwest University, Chongqing, 400715, PR China
[b] College of Chemistry and Materials, Nanning Normal University, Nanning, 530001, PR China

ARTICLE INFO

Keywords:
Electrochemiluminescence
Coreaction accelerator ternary ECL system
G-quadruplex
Regeneration strategy

ABSTRACT

Graphitic carbon nitride nanosheet (g-C_3N_4 NS) with superior photoelectronic properties was served as ECL emitter to in-situ generate Cu@Cu_2O nanoparticles as coreaction accelerator for constructing neoteric ternary ECL system (g-C_3N_4 NS/TEA/Cu@Cu_2O system). Impressively, compared to individual g-C_3N_4 NS, the designed Cu@Cu_2O/g-C_3N_4 NS not only displayed an enhanced current intensity with advance onset potential, but also observed a strong ECL response, which reduced the ECL potential down to 1.3 V for beneficial construction of biosensor, owe to the significant role of Cu@Cu_2O in accelerating the reaction between g-C_3N_4 NS and trimethylamine (TEA). Notably, the enzyme-free target induced recycle amplification was performed to produce two different kinds of single stranded DNAs labeled with ferrocene (Fc, quencher) for the formation of G-quadruplex. Herein, based on the strong ECL signal deriving from the ternary ECL system as a "switch on" mode, and a weak ECL signal due to the co-quenching pattern of ferrocene and hemin as a "switch off" mode, an original "on-off" ECL biosensing platform was developed to ultrasensitively detect microRNA-21. Furthermore, the reversible formation and dissociation of G-quadruplex could achieve the regeneration of ECL biosensor in a rapid step with the aid of potassium ion (K^+) and 18-crown-6-ether. In addition, the developed strategy exhibited a great sensitivity with a detection limit of 48 aM to pave a path for real applications of biomolecules detection in clinical diagnosis.

1. Introduction

Based on the electron confinement in two dimension (2D) (Geim and Novoselov, 2007), the ultrathin 2D nanomaterials with sheet-like structures possess unique and versatile properties in physical, electronic, and chemical fields to achieve a variety of applications, such as catalysis (Deng et al., 2016; Gao et al., 2019), electronics (Wang et al., 2012; Zhang et al., 2018a), sensors (Lu et al., 2009; Wang et al., 2019a), energy storage (Cao et al., 2016; Xia et al., 2018), and biomedicines (Dai et al., 2017; Peng et al., 2018). As the further research on ultrathin 2D nanomaterials, the family members are growing in number, including graphitic carbon nitride (Liu et al., 2019a), hexagonal boron nitride (hBN) (Song et al., 2018), 2D metal-organic frameworks (MOFs) (Rui et al., 2018), transition metal dichalcogenides (TMDs) (Ciarrocchi et al., 2018), covalent-organic frameworks (COFs) (Zhao et al., 2018), black phosphorus (BP) (Zhu et al., 2018), etc. Impressively, g-C_3N_4 nanosheet (NS) with good water dispersity, and high fluorescence quantum yield, has been widely used in biosensing field (Zhang et al., 2012; Vázquez-González et al., 2017; Liu et al., 2019b), such as electrochemiluminescence (ECL) biosensing platforms which exhibited glorious advantages of remarkable controllability, high sensitivity, and low background (Ji et al., 2017). Normally, the strong ECL emission of g-C_3N_4 NS stemmed from the reductive-oxidation ECL type with peroxydisulfate ($S_2O_8^{2-}$) as coreactant (Lv et al., 2018). Whereas, the strong oxidative radical ($SO_4^{\bullet-}$) with a standard potential of E ($SO_4^{\bullet-}/SO_4^{2-}$) = 2.4 V (*vs* NHE) (Rajh et al., 1992) is harmful to biological systems, therefore, it is crucial to explore the oxidative-reduction ECL type of g-C_3N_4 with mild reductive substances as coreactants for decreasing the damage to

* Corresponding author.
** Corresponding author.
E-mail addresses: qi.xiao@nnnu.edu.cn (Q. Xiao), yuanruo@swu.edu.cn (R. Yuan).

https://doi.org/10.1016/j.bios.2020.112006
Received 17 November 2019; Received in revised form 19 December 2019; Accepted 3 January 2020
Available online 7 January 2020

bioassay. However, in the traditional studies on the oxidative-reduction ECL response of the g-C_3N_4, the positive ECL potential was performed to more than 1.6 V with a massive doses of coreactant, which might cause the electrolysis of aqueous solution to introduce more interference (Cheng et al., 2013; Wang et al., 2016). Recently, to achieve the enhancement of the anodic ECL intensity, the introduction of coreaction accelerator in the oxidative-reduction ECL system has constituted a ternary ECL system by effectively increasing the production of free radicals of coreactant to react with ECL emitter for an intense ECL signal (ZhangLi et al., 2019). In this work, the Cu@Cu_2O nanoparticles (NPs) as coreaction accelerator was in-situ grew on g-C_3N_4 NS with triethylamine (TEA) as coreactant to construct an excellent ternary ECL pattern, which not only tremendously improved the anodic ECL signal of g-C_3N_4 NS for enhancing the detection sensitivity, but also reduced the ECL potential down to 1.3 V for maintaining biomolecular activity to construct a biofriendly biosensing platform.

MicroRNAs (miRNAs), as a predominant regulator in gene expression, are a series of short non-coding RNAs (20–24 nucleotides) (Friedman et al., 2009). Severely, the anomalous expression of miRNAs is closely related to several malignant diseases (such as cancer, cardiovascular disease, etc.) (Lin and Gregory, 2015; Majd et al., 2018). Therefore, the sensitive detection of miRNAs as tumor biomarkers is expected to realize the early diagnosis of disease. Recently, ECL biosensing platform based on nucleic acid amplification strategy has attracted increasing attention to achieve ultrasensitive detection of biomolecules (Wang et al., 2019). Compared to the enzyme-driven DNA amplification strategies (rolling circle amplification (Yang et al., 2016), enzyme-mediated strand replacement amplification (Lei et al., 2018), enzyme induced cleavage reaction (Zhao et al., 2019)) with harsh reaction temperature and high detection cost, the enzyme-free target induced recycle amplification (ETIRA) exports mimic target in a 1:N ratio pattern with the participation of toehold-mediated strand displacement reaction (SDR) in room temperature (Zhang et al., 2018b). Nevertheless, the above strategy produces one mimic target resulting in the waste of another DNA in one circle of target recycling. Herein, two different kinds of single stranded DNAs originating from the ETIRA were applied to form G-quadruplex, which eliminated the waste of DNA and implemented the reversible formation and dissociation of G-quadruplex with the aid of potassium ion (K^+) and 18-crown-6-ether (Hu et al., 2014) for further construction of regeneration ECL biosensing platform.

Inspired by the configuration transformation of G-quadruplex, a regenerated ECL biosensing platform was constructed based on the ternary ECL system (g-C_3N_4 NS/TEA/Cu@Cu_2O system) and DNA amplification strategy (ETIRA) to achieve ultrasensitive miRNA-21 detection. Herein, the principle in the preparation of Cu@Cu_2O/g-C_3N_4 NS and the construction of ECL biosensing platform are depicted in Scheme 1. Firstly, the g-C_3N_4 nanosheet (NS) was obtained by ultrasonic stripping of bulk g-C_3N_4 to further in situ reduce Cu@Cu_2O NPs on its surface for the generation of Cu@Cu_2O/g-C_3N_4 NS (PART A). Significantly, the ternary ECL system exhibited an intense ECL response and a lower ECL potential at 1.3 V, with g-C_3N_4 NS as ECL emitter, TEA as coreactant and Cu@Cu_2O NPs as coreaction accelerator. Then, the capture DNA (CP) labeled with amino (-NH_2) group was connected on the decorated glassy carbon electrode (GCE) *via* the Cu–N coordinate bond (PART B).

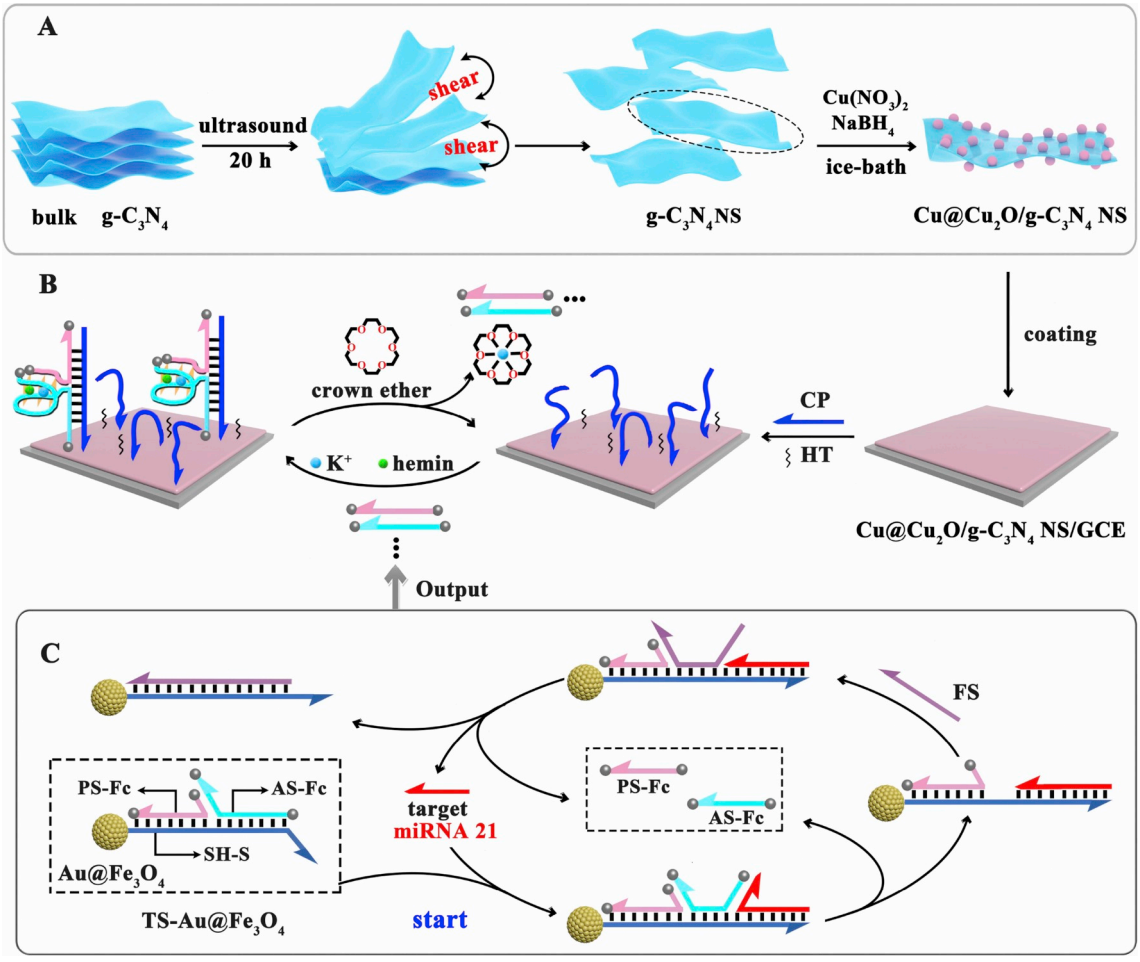

Scheme 1. The schematic diagram of (A) the production of Cu@Cu_2O/g-C_3N_4 NS; (B) the construction of ECL biosensing platform. (C) the principle of enzyme-free target induced recycle amplification.

Subsequently, the ETIRA was carried out to export plentiful of single-stranded DNA tagged with ferrocene (PS-Fc, AS-Fc) (the PAGE analysis was shown in the Supporting information (Fig. S1)). As shown in Part C, initially, the TS-Au@Fe_3O_4 was assembled from three single strands DNA (SH–S, PS-Fc, AS-Fc) with Fe_3O_4 NPs for the three dimensional (3D) reactor. With the aid of target miRNA-21, the toehold-mediated strand displacement reaction was occurred in the presence of DNA fuel (FS) to release miRNA-21 for target cycle amplification, and PS-Fc, AS-Fc for further biosensor construction. After magnetic separation, the solution containing PS-Fc, AS-Fc was incubated on the electrode to generate hemin/G-quadruplex with the help of K^+ and hemin, which exhibited the co-quenching mode of Fc and hemin/G-quadruplex DNAzyme to reduce ECL signal ("signal off" mode). Notably, when the electrode was incubated with crown ether solution, the G-quadruplex fell off the electrode to achieve the regeneration of the biosensing system due to the ion-recognition between crown ether and K^+ in a rapid way. In consequence, the developed ECL biosensor provided a promising strategy to quantify target miRNA-21 with a low detection limit of 48 aM. Significantly, this protocol exhibits novel ideas in the construction of new biosensing platforms to achieve biomolecules analysis for early cancer diagnosis.

2. Results and discussion

2.1. Morphology characterizations of Cu@Cu_2O/g-C_3N_4 NS

Herein, scanning electron microscope (SEM) and transmission electron microscopy (TEM) were applied to verify the formations of the g-C_3N_4 nanosheets (NS) and Cu@Cu_2O/g-C_3N_4 NS. Fig. 1A depicted the SEM image of bulk g-C_3N_4, exhibiting a massive multilayer structure with a rough size of 2 μm. After exfoliating the bulk g-C_3N_4 by ultrasound, the lamellar fold g-C_3N_4 NS was obtained with wavy sheet, as shown in Fig. 1B. When the Cu@Cu_2O was in-situ reduced on the g-C_3N_4 NS, the HRTEM picture of Cu@Cu_2O/g-C_3N_4 NS showed that small spheres with homogeneous diameter of about 5 nm were distributed uniformly on the g-C_3N_4 NS (Fig. 1C). Furthermore, the amplified HRTEM image of Cu@Cu_2O presented the crystal information. As shown in Fig. 1D, the lattice spacing with 0.25 nm belongs to (111) plane of Cu_2O, while the lattice fringes with spacing of 0.21 nm could be indexed to the lattice facets of Cu (111). Besides, X-ray photoelectron spectroscopy (XPS) was further executed to investigate elemental analysis of the Cu@Cu_2O/g-C_3N_4 NS in the Supporting information (Fig. S2). According to Fig. S2A, the XPS spectra of full range clearly exhibited the characteristic peaks of C 1s, N 1s, O 1s, Cu 2p, CuLM2 regions. Furthermore, the characteristic peaks of the Cu 2p (Fig. S2C) at 932.6 eV (Cu 2p3/2) and 952.8 eV (Cu 2p1/2) were manifested the generation of Cu_2O particles. Meanwhile, the Cu LM2 peaks at 568.1 and 571.5 eV (Fig. S2D) were observed to distinguish the Cu^0 and Cu_2O, which demonstrated the successful generation of Cu@Cu_2O on the g-C_3N_4 NS.

2.2. Optical characterizations of Cu@Cu_2O/g-C_3N_4 NS

The optical properties of the Cu@Cu_2O/g-C_3N_4 NS were characterized by the UV–vis diffuse reflection, fluorescence (FL) and ECL spectra, respectively. As profiled in Fig. 2A, the individual g-C_3N_4 NS depicted an absorption edge at about 450 nm (curve a). Compared to the absorption of individual g-C_3N_4, the absorptions of Cu@Cu_2O/g-C_3N_4 NS (curve b) on the visible region increased distinctly with a slight red shift (10 nm), after the Cu@Cu_2O was in-situ reduced on the g-C_3N_4 NS. In addition, the g-C_3N_4 NS showed almost pale ivory under visible light while emitted light blue fluorescence with excited irradiation of 365 nm by a UV lamp (the inset of Fig. 2A). Fig. 2B displayed the maximum FL emission wavelength of the Cu@Cu_2O/g-C_3N_4 NS at 438 nm (curve a). Interestingly, the maximum emission wavelength on ECL spectra of Cu@Cu_2O/g-C_3N_4 NS with TEA as coreactant exhibited a large red-shifted (172 nm) than that of the FL emission of the Cu@Cu_2O/g-C_3N_4 NS, which attributed to the surface state transition of the Cu@Cu_2O/g-C_3N_4 NS (Liu et al., 2019c). In addition, as depicted in the ECL 3D color map surface (Fig. 2C), the ECL emission evolution process was traced with the cyclic voltage scanning from 0 V to 1.3 V and back to 0 V. Furthermore, the ECL heat map image (Fig. 2D) exhibited a wide emission range from 500 to 750 nm with a maximum ECL emission wavelength at 610 nm.

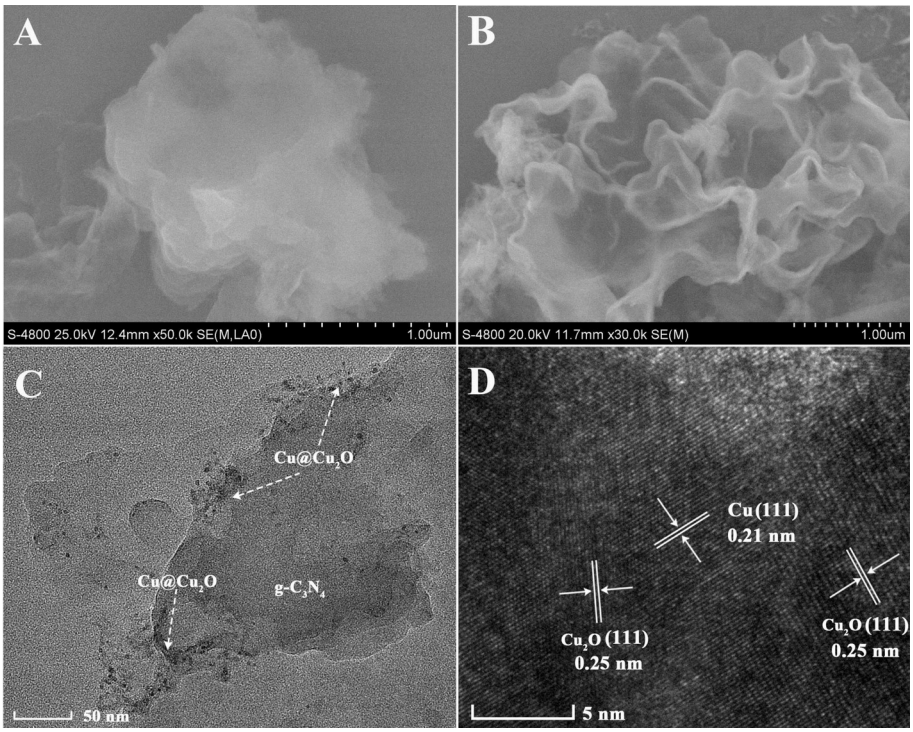

Fig. 1. The SEM images of (A) bulk g-C_3N_4 and (B) g-C_3N_4 NS. (C) HRTEM image of Cu@Cu_2O/g-C_3N_4 NS, and (D) the amplified HRTEM image of Cu@Cu_2O.

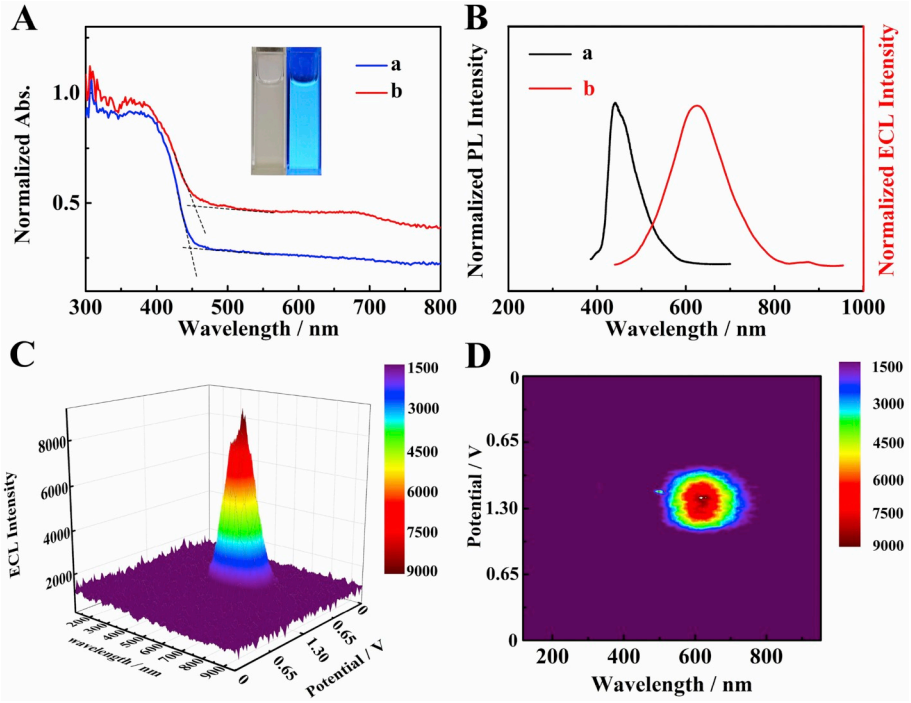

Fig. 2. (A) UV–vis diffuse reflectance spectra of the individual g-C_3N_4 NS (a), and the Cu@Cu_2O/g-C_3N_4 NS (b). (B) FL spectra of Cu@Cu_2O/g-C_3N_4 NS (a), ECL spectra of Cu@Cu_2O/g-C_3N_4 NS in PBS containing 18 mM TEA (b). The ECL 3D color map (C) and the ECL heat map (D) of Cu@Cu_2O/g-C_3N_4 NS in PBS containing 18 mM TEA. (For interpretation of the references to color in this figure legend, the reader is referred to the Web version of this article.)

2.3. ECL emission and quenching mechanism of Cu@Cu_2O/g-C_3N_4 NS

The ECL luminescence mechanism of diverse luminescent g-C_3N_4 nanomaterials was demonstrated by executing relative ECL and differential pulse voltammetry (DPV) experiments. As depicted in Fig. 3A, compared to the ECL signal (207 a.u.) of bulk g-C_3N_4/GCE in PBS solution (curve a'), the g-C_3N_4 NS/GCE exhibited the ECL intensity of 1103 a.u. (curve a), which is 5-fold higher than the ECL signal of bulk g-C_3N_4 because of the large specific surface of thin layer g-C_3N_4 enhancing electronic transmission performance. When the Cu@Cu_2O was in-situ reduced on the g-C_3N_4 NS, the individual Cu@Cu_2O/g-C_3N_4 NS exhibited the ECL signal of 1527 a.u. (curve c), which was more intense than that of g-C_3N_4 NS. Simultaneously, compared to the DPV curve of g-C_3N_4 NS with unconspicuous redox peak (curve a, Fig. 3B), the Cu@Cu_2O/g-C_3N_4 NS showed stronger current intensity (curve b), attributing to the good electrical conductivity of Cu@Cu_2O for enhancement of electron transmission. Specifically, after the g-C_3N_4 NS/GCE was scanned in PBS solution with 18 mM trimethylamine (TEA) to form a traditional binary g-C_3N_4/TEA ECL system, the ECL intensity reached to 7639 a.u. (curve c). Meanwhile, the oxidation current (curve c, Fig. 3B) dramatically increased when the onset potential was about 0.7 V due to the oxidation of TEA to produce TEA radical cation ($TEA^{\bullet+}$) and further dehydrogenate to form strong reductant $TEA^{\bullet}$. Obviously, after the introduction of Cu@Cu_2O into the g-C_3N_4/TEA system, the ECL signal of Cu@Cu_2O/g-C_3N_4 NS zoomed to 17080 a.u. (curve d, Fig. 3A). To further explore the possible ECL enhancement mechanism of Cu@Cu_2O/g-C_3N_4 NS, the DPV measurement was executed. As depicted in the curve d of Fig. 3B, the onset potential of the increased oxidation current located at around 0.65 V, which was 0.05 V ahead than that of the g-C_3N_4 NS/GCE scanning in PBS solution with 18 mM TEA. Simultaneously, the current intensity of Cu@Cu_2O/g-C_3N_4 NS was quite stronger than that of g-C_3N_4 NS, which ascribed to the generation of more active radical $TEA^{\bullet}$ from the reaction between the Cu@Cu_2O and TEA to react with g-$C_3N_4^{\bullet+}$ for abundant g-C_3N_4* in the ternary ECL

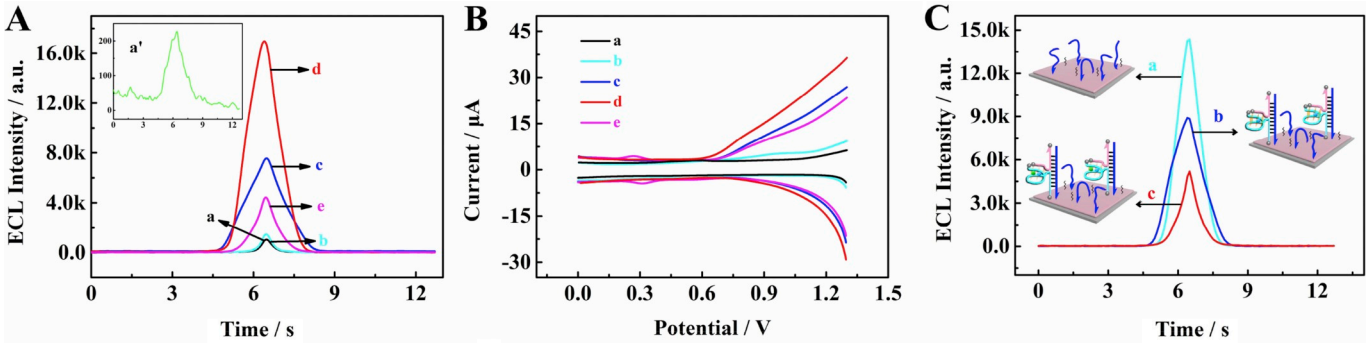

Fig. 3. (A) The ECL intensity curves and (B) DPA curves of (a) g-C_3N_4 NS/GCE in PBS solution, (a') bulk g-C_3N_4/GCE in PBS solution, (b) Cu@Cu_2O/g-C_3N_4 NS/GCE in PBS solution, (c) g-C_3N_4 NS/GCE in PBS solution containing 18 mM TEA, (d) Cu@Cu_2O/g-C_3N_4 NS/GCE in PBS solution containing 18 mM TEA. and (e) the proposed biosensor incubated with sample solution (containing 1 pM miRNA-21) in PBS solution containing 18 mM TEA. (C) ECL intensities of the developed biosensor in (a) PBS solution + 18 mM TEA, (b) PBS solution + 18 mM TEA + sample solution (containing 1 pM miRNA-21), (c) PBS solution + 18 mM TEA + sample solution (containing 1 pM miRNA-21 and 0.5 μM hemin).

system with g-C_3N_4 NS as luminophore, TEA as coreactant and Cu@Cu_2O as coreaction accelerator. The possible ECL mechanism of the ternary ECL system of Cu@Cu_2O/g-C_3N_4 NS/TEA was listed in eq 1 - eq 5 of the Supporting information (Fig. S3).

Obviously, when the proposed ECL biosensor was incubated with sample solution containing 1 pM miRNA-21, the ECL signal was extremely decreased to 4458 a.u. (curve e, Fig. 3A). Furthermore, the characteristic peak of Fc was appeared at around 0.3 V, due to the oxidation of Fc (II) to Fc (III) upon the anode scanning (eq 6). Subsequently, Fc (III) could react with $TEA^{\bullet}$ (eq 7) to consume the active radical for the significant reduction of the oxidation current (curve e, Fig. 3B). Meanwhile, the amount of excited state g-C_3N_4 * was further decreased by the co-quenching pattern in the presence of Fc (III) and Hemin (Fe III)/DNAzyme (eq 8 and eq 9), which caused the quenching of ECL response (eq 6 - eq 9 were listed in Fig. S3 of Supporting information).

Furthermore, to explore the function of hemin/G-quadruplex DNAzyme in the ECL biosensing platform, the ECL responses of proposed ECL biosensor incubating with different sample solutions were measured under the same conditions with 1 pM miRNA-21. As shown in Fig. 3C, the proposed biosensor without sample solution exhibited an intense ECL response of 14357 a.u. (curve a), attributing to the ternary ECL system (g-C_3N_4 NS/TEA/Cu@Cu_2O system). When the modified GCE was incubated with sample solution (no hemin) to generate G-quadruplex labeled with Fc, the ECL response of the biosensor dropped to 8902 a.u. (curve b) because of the quenching effect of Fc. However, after hemin was introduced to the G-quadruplex for the development of hemin/G-quadruplex DNAzyme, the ECL intensity decreased much more obviously (4458 a.u., curve c), because of co-quenching mode of Fc and hemin/DNAzyme.

2.4. Electrochemical performance of the ECL biosensor

The assembly courses of the proposed ECL biosensor were evaluated by cyclic voltammetry (CV) and EIS characterization in 5.0 mM $[Fe(CN)_6]^{3-/4-}$ solution with 0.1 M KCl. As depicted in Fig. S4A, compared to the redox current of the bare GCE (curve a), the current signal (curve b) of electrode modified with Cu@Cu_2O/g-C_3N_4 enhanced observably, due to the excellent electron transfer capacity of the Cu@Cu_2O. After the assembly of capture DNA (CP) on the modified GCE, the redox peak currents exhibited significant decrease (curve c), ascribing to the electron hindrance of DNA with negative charge. When the modified GCE was blocked with HT, the CV current sequentially decreased (curve d) because the HT impeded the electron transfer. Ultimately, after the introduction of PS-Fc, AS-Fc on the electrode to form the G-quadruplex, the CV current further reduced on account of the obstruction of DNA monolayer.

To further demonstrate the stepwise assembly of the electrode, the EIS characterization was executed with $[Fe(CN)_6]^{3-/4-}$ as redox probe. As profiled in curve a of Figs. S4B and a small semicircle domain of bare GCE was obtained on account of the relatively low electron transfer resistance (R_{et}) of smooth surface. After the GCE was modified with Cu@Cu_2O/g-C_3N_4, the R_{et} decreased slightly (curve b), attributing to the acceleration of electron transfer on the Cu@Cu_2O/g-C_3N_4 surface. When the CP was covalently bound on the surface of modified GCE, the diameter of semicircle increased (curve c) due to the insulation of negatively charged DNA backbones. After decoration with HT, the R_{et} of electrode continually increased (curve d), which attributed to the obstruction of HT. As expected, the resistance further enhanced (curve e) after the PS-Fc and AS-Fc were incubated on the modified GCE on account of the impediment of G-quadruplex.

2.5. ECL response of the developed biosensor

To investigate the sensitivity of the developed biosensor, the quantitative measurements with different concentration of microRNA-21 (miRNA-21) were performed in PBS (pH 7.4) involving 18 mM TEA. As depicted in Fig. 4A, with the increment of miRNA-21 from 100 aM to 100 pM, the ECL intensities gradually decreased. Furthermore, the calibration plot (Fig. 4B) showed a good linear relationship between the changes of ECL response (ΔI_{ECL}) and the logarithm of miRNA-21 with the regression equation $\Delta I_{ECL} = 2009.94 \lg c + 9058.41$. Simultaneously, the limit of detection (LOD) was calculated as 48 aM ($S/N = 3$). In addition, the proposed biosensors showed good sensitivity for the determination of miRNA-21 compared to other assays listed in Table S2, and the applicability of the proposed biosensor was evaluated in the lysates of cells (the result was shown in the Supporting information).

2.6. Selectivity, stability and regenerability of the ECL biosensing platform

To evaluate the ECL properties of the proposed biosensor, selectivity and stability were investigated consecutively. Therefore, the interference experiments were executed on the ECL biosensor to study the selectivity by incubating with interfering microRNAs (including miRNA-141, miRNA-155, miRNA-199a). As shown in Fig. 5A, 100 pM of miRNA-141, miRNA-155 and miRNA-199a were used to substitute the target miRNA-21 (1 pM), respectively, which caused a slight ECL decrease compared to that of the blank sample (without target). However, the ECL response of the as-prepared ECL biosensor incubating with the mixture solution (1 pM miRNA-21 and 100 pM interfering microRNAs) approximated to the ECL signal with 1 pM miRNA-21, which certified that the miRNA-141, miRNA-155, miRNA-199a exhibited no significant effect with miRNA-21, suggesting a good specificity and selectivity of the proposed ECL biosensor. Subsequently, the ECL intensity of the developed biosensor was measured by consecutive ECL scans of 13 cycles with 1 fM miRNA-21 to assess the stability. As profiled in Fig. 5B, the ECL intensities of the proposed biosensor showed slight changes and the relative standard deviation (RSD%) of 1.57%, demonstrating admirable stability of the developed biosensor. Furthermore, the regenerability of the proposed biosensor for the detection of miRNA-21 was explored as depicted in Fig. 5C. The first intense ECL signal on the top denoted the "signal-on" state of the proposed biosensor as blank ECL response. When the ECL biosensor was incubated with sample solution containing 1 pM miRNA-21, the ECL response declined rapidly for a "signal-off" state, due to the co-quenching mode of Fc and hemin/G-quadruplex DNAzyme. After incubated with 18-crown-6-ether, the G-quadruplex dissociated to recover an intense ECL signal (97% of the blank ECL intensity) attributing to the ion recognition between K^+ and 18-crown-6-ether. Furthermore, the proposed "on-off" mode ECL biosensor was switched sensitively to monitor miRNA-21 over 3 cycles, which indicated a satisfactory regeneration ability for miRNA-21 detection.

3. Conclusions

In this protocol, we have developed a regenerable ECL biosensing platform based on the ternary ECL system (g-C_3N_4 NS/TEA/Cu@Cu_2O) and enzyme-free target induced recycle amplification (ETIRA) for ultrasensitive microRNA-21 (miRNA-21) detection. Significantly, the Cu@Cu_2O nanoparticles as coreaction accelerator dramatically improved the reaction rate of the g-C_3N_4 NS and TEA to obtain an intense ECL signal for "signal-on" state. With the aid of target miRNA-21, two different kinds of single stranded DNAs labeled with ferrocene (Fc) were outputted from the ETIRA for the generation of G-quadruplex in the aid of potassium ion (K^+). Remarkably, the co-quenching pattern of Fc and hemin/DNAzyme caused a declined ECL intensity as a "signal-off" state. On basis of the ion-recognition between K^+ and 18-crown-6-ether, the designed G-quadruplex could be rapidly reverse for the regenerable ECL biosensing platform. In view of these advantages, the proposed strategy exhibits an efficient scheme for the ultrasensitive detection of biomolecules in clinical diagnosis.

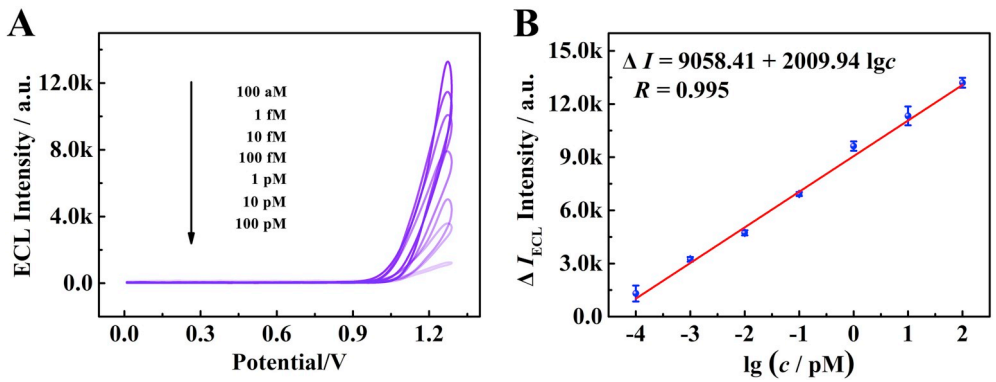

Fig. 4. (A) ECL profiles of the ECL biosensor with various concentrations of miRNA-21. (B) Calibration plot between the changes of ECL signal (ΔI_{ECL}) and the logarithm of miRNA-21 concentrations. Error bars, standard deviation (SD), $n = 3$.

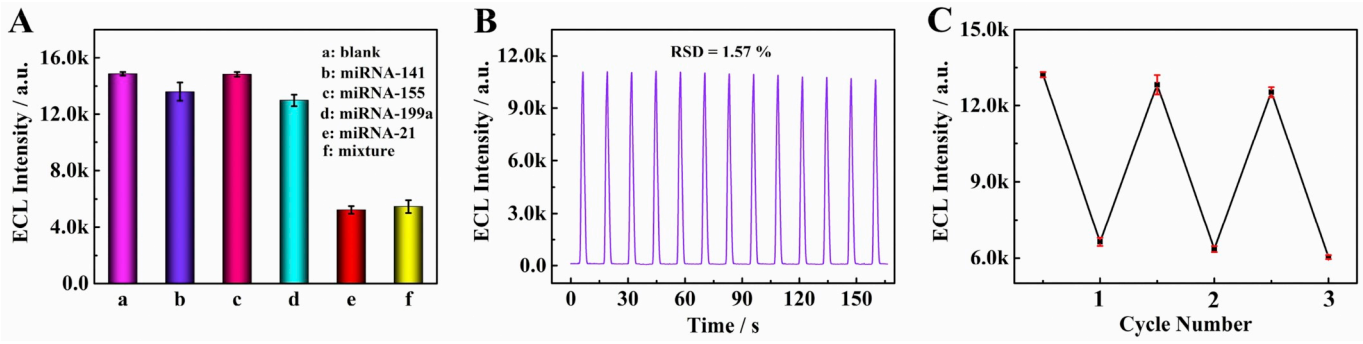

Fig. 5. (A) Selectivity of the ECL biosensor for diverse miRNAs: (a) blank (without target miRNA-21), (b) 100 pM miRNA-141, (c) 100 pM miRNA-155, (d) 100 pM miRNA-199a, (e) 1 pM miRNA-21, (f) the mixture (containing miRNA-21, miRNA-141, miRNA-155, miRNA-199a, respectively). (B) Stability of the ECL biosensor with 1 fM miRNA-21 by continuous scanning. (C) The regeneration test of the proposed biosensor for three cycles.

Declaration of competing interest

The authors declare that they have no known competing financial interests or personal relationships that could have appeared to influence the work reported in this paper.

CRediT authorship contribution statement

Jia-Li Liu: Conceptualization, Data curation, Formal analysis, Investigation, Writing - original draft, Writing - review & editing. **Jie Jiang:** Data curation, Formal analysis, Investigation. **Jia-Qi Zhang:** Data curation, Investigation. **Ya-Qin Chai:** Funding acquisition, Resources, Project administration, Supervision. **Qi Xiao:** Funding acquisition, Resources, Project administration, Supervision. **Ruo Yuan:** Funding acquisition, Resources, Writing - review & editing.

Acknowledgements

This work was financially supported by the NNSF of China (21974108, 21675129, 21775124, 21763005) and the Fundamental Research Funds for the Central Universities (XDJK2019TJ002), China.

Appendix A. Supplementary data

Supplementary data to this article can be found online at https://doi.org/10.1016/j.bios.2020.112006.

References

Cao, X.H., Tan, C.L., Zhang, X., Zhao, W., Zhang, H., 2016. Adv. Mater. 28, 6167–6196.
Cheng, C., Huang, Y., Wang, J., Zheng, B., Yuan, H., Xiao, D., 2013. Anal. Chem. 85, 2601–2605.
Ciarrocchi, A., Avsar, A., Ovchinnikov, D., Kis, A., 2018. Nat. Commun. 9, 919.
Dai, C., Zhang, S., Liu, Z., Wu, R., Chen, Y., 2017. ACS Nano 11, 9467–9480.
Deng, D., Novoselov, K.S., Fu, Q., Zheng, N., Tian, Z., Bao, X., 2016. Nat. Nanotechnol. 11, 218–230.
Friedman, R.C., Farh, K.K., Burge, C.B., Bartel, D.P., 2009. Genome Res. 19, 92–105.
Gao, K., Wang, B., Tao, L., Cunning, B.V., Zhang, Z., Wang, S., Ruoff, R.S., Qu, L., 2019. Adv. Mater. 31, 1805121.
Geim, A.K., Novoselov, K.S., 2007. Nat. Mater. 6, 183–191.
Hu, L., Liu, X., Cecconello, A., Willner, I., 2014. Nano Lett. 14, 6030–6035.
Ji, J., Wen, J., Shen, Y., Lv, Y., Chen, Y., Liu, S., Ma, H.B., Zhang, Y., 2017. J. Am. Chem. Soc. 139, 11698–11701.
Lei, Y.M., Zhou, J., Chai, Y.Q., Zhuo, Y., Yuan, R., 2018. Anal. Chem. 90, 12270–12277.
Lin, S., Gregory, R.I., 2015. Nat. Rev. Cancer 15, 321–333.
Liu, J., Zhang, Y., Zhang, L., Xie, F., Vasileff, A., Qiao, S.Z., 2019a. Adv. Mater. 31, 1901261.
Liu, J.L., Zhang, J.Q., Tang, Z.L., Zhuo, Y., Chai, Y.Q., Yuan, R., 2019c. Chem. Sci. 10, 4497–4501.
Liu, X.T., Zhang, H.J., Song, Z.P., Guo, L.Q., Fu, F.F., Wu, Y.N., 2019b. Biosens. Bioelectron. 129, 118–123.
Lu, C.H., Yang, H.H., Zhu, C.L., Chen, X., Chen, G.N., 2009. Angew. Chem. Int. Ed. 48, 4785–4787.
Lv, Y., Chen, S., Shen, Y., Ji, J., Zhou, Q., Liu, S., Zhang, Y., 2018. J. Am. Chem. Soc. 140, 2801–2804.
Majd, S.M., Salimi, A., Ghasemi, F., 2018. Biosens. Bioelectron. 105, 6–13.
Peng, L., Mei, X., He, J., Xu, J., Zhang, W., Liang, R., Wei, M., Evans, D.G., Duan, X., 2018. Adv. Mater. 30, 1707389.
Rajh, T., Saponjic, Z.V., Micic, O.I., 1992. Langmuir 8, 1265–1270.
Rui, K., Zhao, G., Chen, Y., Lin, Y., Zhou, Q., Chen, J., Zhu, J.X., Sun, W.P., Huang, W., Dou, S.X., 2018. Adv. Funct. Mater. 28, 1801554.
Song, Y., Mandelli, D., Hod, O., Urbakh, M., Ma, M., Zheng, Q., 2018. Nat. Mater. 17, 894–899.
Vázquez-González, M., Liao, W.C., Cazelles, R., Wang, S., Yu, X., Gutkin, V., Willner, I., 2017. ACS Nano 11, 3247–3253.
Wang, B.X., Wang, H.J., Zhong, X., Chai, Y.Q., Chen, S.H., Yuan, R., 2016. Chem. Commun. 52, 5049–5052.
Wang, C.X., Chen, L.M., Wang, P.J., Li, M.S., Liu, D.F., 2019. Biosens. Bioelectron. 133, 154–159.

Wang, Q.H., Kalantar-Zadeh, K., Kis, A., Coleman, J.N., Strano, M.S., 2012. Nat. Nanotechnol. 11, 699–712.
Wang, Z., Yi, K., Lin, Q., Yang, L., Chen, X., Chen, H., Liu, Y.Q., Wei, D., 2019a. Nat. Commun. 10, 1544.
Xia, Y., Mathis, T.S., Zhao, M.Q., Anasori, B., Dang, A., Zhou, Z., Cho, H., Gogotsi, Y., Yang, S., 2018. Nature 557, 409–412.
Yang, L., Tao, Y., Yue, G., Li, R., Qiu, B., Guo, L., Lin, Z.Y., Yang, H.H., 2016. Anal. Chem. 88, 5097–5103.
Zhang, N., Shi, X.M., Guo, H.Q., Zhao, X.Z., Zhao, W.W., Xu, J.J., Chen, H.Y., 2018b. Anal. Chem. 90, 11892–11898.
Zhang, Q., Chu, L., Zhou, F., Ji, W., Eda, G., 2018a. Adv. Mater. 30, 1704055.
Zhang, X., Xie, X., Wang, H., Zhang, J., Pan, B., Xie, Y., 2012. J. Am. Chem. Soc. 135, 18–21.
Zhang, X.L., Li, W.M., Zhou, Y., Chai, Y.Q., Yuan, R., 2019. Biosens. Bioelectron. 135, 8–13.
Zhao, C., Diercks, C.S., Zhu, C., Hanikel, N., Pei, X., Yaghi, O.M., 2018. J. Am. Chem. Soc. 140, 16438–16441.
Zhao, R.N., Jia, L.P., Feng, Z., Ma, R.N., Zhang, W., Shang, L., Xue, Q.W., Wang, H.S., 2019. Biosens. Bioelectron. 144, 111669.
Zhu, M., Sun, Z., Fujitsuka, M., Majima, T., 2018. Angew. Chem. Int. Ed. 57, 2160–2164.